Geomechanical Analysis of Caprock and Fault Stability in a Full 3D Field Model During CO₂ Geological Storage

Enyi Yu*[1], Shilong Liu[1], Zongyang Li[2], Dong Zhang[2], Hui Wu[3], Yuan Di[1], 1. College of Engineering, Peking University, 2. Exploration and Development Research Institute, Shengli Oilfield Company, SINOPEC, 3. School of Earth and Space Science, Peking University.

Abstract

Objectives and Scope: Injecting carbon dioxide (CO_2) into the formation results in fluid pressure accumulation, leading to changes in the effective stress field. Stress changes can activate preexisting faults, compromise sealing behavior of caprock, and trigger ground surface uplift. Therefore, conducting mechanical analysis and stability assessment is crucial for the successful industrial implementation of CO_2 geological storage.

Methods, Procedures, Process: The Gao89-1 block of Shengli Oilfield is the target site in this study. A full 3D field model of Gao89-1 block was constructed using hexahedral finite elements. The changes in fluid pressure and the stress evolution during CO_2 injecting were simulated and analyzed. Caprock stability and fault reactivation were assessed based on Mohr-Coulomb criterion. For caprocks, a safety factor was employed to assess the trend of failure. Similarly, the stability of faults was determined using the Coulomb failure function.

Results, Observations, Conclusions: To accurately simulate the stress distribution, it is essential to convert the corner-point grid of the target geological model into a standard finite element mesh. This process involves reading the target reservoir model and faults data, aligning the vertices of grids, handling degenerate grids, assigning valid depth to invalid grids, geometric optimization, domain extension, and fault embedding or equivalence. As CO_2 is injected, both fluid pressure and shear stress gradually increase injection time, while the mean effective stress gradually decreases. Consequently, the stress state

tends towards the failure envelope, increasing the risk of shear failure. However, once the injection is halted, the stress state moves backward, but stabilizes to the left of the initial stress state. Through calculating the safety factor, it has been determined that the formation remains in a relatively safe and stable state, with an expected absence of shear failure. This favorable condition can be attributed to the implementation of a relatively low injection rate and the careful selection of simulation parameters.

Significance/Novelty: A workflow for converting the corner-point grid of the target geological model into a standard finite element mesh for a full 3D field model has been developed. The geomechanical response in the Gao89-1 block of the Shengli oilfield has been analyzed, providing a valuable reference for further studies on CO_2 geological storage at the site scale.

Introduction

Carbon dioxide (CO_2) is widely recognized as a significant greenhouse gas. Due to its excessive emissions, the atmospheric concentration of CO_2 continues to rise, causing global climate change and posing a severe threat to the human living environment (Aminu et al. 2017). To mitigate the accumulation of CO_2 in the atmosphere, Carbon Capture, Utilization, and Storage (CCUS) has emerged as a promising approach (Legentil et al. 2023, Newell and Martinez 2020, Zheng et al. 2021). The Qilu-Shengli Oilfield CCUS project, completed by SINOPEC, is China's first megaton CCUS project, with the aim of reducing carbon emissions by 1 million tons per year.

Within the field of CCUS, CO_2 geological storage specifically focuses on the secure and long-term storage of CO_2 in deep geological formations. Potential storage sites include deep sedimentary formations such as oil and gas reservoirs and deep saline aquifers (Pan et al. 2016, Legentil et al. 2023). The low-permeability caprock and faults ensure the containment for structural trapping of CO_2 within the target formation (Sun et al. 2023). However, the injection of CO_2 can induce stress changes, which may activate preexisting faults, compromise the integrity of the caprock, trigger seismic activity, and cause surface uplift (Sun et al. 2023, Raziperchikolaee and Pasumarti 2020). It should be noted that the highest risk of creating a pathway for fluid leakage occurs during or immediately after fault reactivation or caprock failure. Therefore, understanding the geomechanical analysis and stability assessment of caprock and faults is crucial in the site selection for commercial CO_2 storage.

Numerical simulation is a valuable tool for predicting the geomechanical response and assessing the likelihood of the aforementioned issues. Yoon et al. (2023) developed a numerical simulator that coupled a multiphase flow simulator RS-CO2 with the geomechanics simulator FLAC 3D to investigate the potential activation and slip of faults during CO_2 geological storage. Hettema (2020) described a comprehensive methodology to determine the critical reservoir depletion pressure for fault reactivation and derived analytical solutions for different fault categories, including open intra-reservoir faults, sealing intra-reservoir faults, and boundary faults. Adu-Gyamfi et al. (2022) evaluated the chemo-mechanical impact of injected CO_2 on the reservoir and caprock integrity, assessing the long-term CO_2 storage capability. Jin et al. (2023) developed an extended evaluation method of fault stability that considered the heterogeneity in friction strength resulting from variations in clay content within the fault zone. In some simulation studies, the focus is often limited to the reservoir domain due to limited field data. However, it is essential to establish a more comprehensive and reliable full 3D field model to account for the geomechanical response in the caprock and other layers. Furthermore, appropriate criteria, such as the Mohr-Coulomb strength criterion, is necessary to analyze the mechanical stability of faults and caprock. Generally, satisfying the Mohr-Coulomb strength criterion is generally considered the first necessary condition for the occurrence of failure.

In this study, we established a conversion workflow to generate a finite element grid for a full 3D field model from a corner-point grid of the target geological model. The simulations were conducted using the GEOS simulator based on fully coupling of fluid and solid mechanics. The mechanical stability analysis of caprocks and faults was performed based on the Mohr-Coulomb criterion.

The Full 3D Field Model

During the injection of CO_2, fluid flows within the reservoir domain, while the resulting stress changes extend beyond the reservoir to encompass the wider subsurface formations, including the overlying caprock, underlying basement, and surrounding strata, as shown in Figure 1. However, in many cases, there are only geological models available for the reservoir and faults. On the other hand, accurately imposing boundary conditions around the reservoir domain is challenging. Regions distant from the reservoir tend to have relatively stable stress or strain, making them suitable for setting boundary conditions. Moreover, by establishing a full 3D field model, the effects of boundaries can be mitigated, and errors in boundary conditions can be eliminated, ensuring a more accurate representation of the central region.

Besides, most geological and property models depict the distribution and characteristics of reservoirs using corner-point grids (Liu et al. 2019). Corner points are defined by row, column, and layer indices (i, j, k), allowing for flexibility in modifying unit dimensions and inclining the grid surface that connects top and bottom corner points. This adaptability of corner-point grids enables the accurate representation of faults, pinch-outs, and other irregularities (Chen et al. 2017). However, the use of corner-point grids in simulating the stress field is limited due to the presence of duplicate nodes, which hampers the transmission of continuous variables like force, and displacement. Therefore, to ensure an accurate simulation of the stress distribution, it is essential to transform the corner-point grid of the target geological model into a standard finite element mesh that is non-degenerate, vertex-aligned, and smooth. This conversion allows for the establishment of a finite element grid within a full 3D field model, enabling more reliable simulations of the stress field and facilitating geomechanical analysis during CO_2 geological storage.
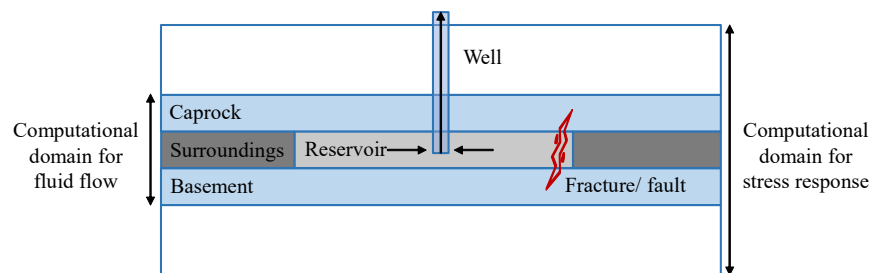

Figure 1. The sketch of the full 3D field model

The establishment of a finite element grid for a full 3D field model involves several basic steps. These steps include:

(1) Reading the target reservoir model and faults data, which are represented as corner-point grid data from Petrel. This is illustrated in Figure 2(a).

(2) Aligning the vertices of grids by taking the midpoints of adjacent cells on the same pillar to ensure vertex alignment. This is shown in Figure 2(b).

(3) Handling degenerate grids that may occur at fault boundaries or pinch-out locations. Adjustments are made to avoid vertex collinearity or coincidence. Figure 2(c) illustrates this adjustment.

(4) Assigning depth values for invalid grids. The depth data of invalid grids in the geological model are given default values and cannot be directly used in finite element simulations. Interpolation is used to assign depth values to establish a continuous depth distribution. Figure 2(d) demonstrates the assignment process.

(5) Geometric optimization. To enhance the orthogonality and continuity of the grids, the Laplace smoothing method is applied. This technique averages the local neighborhood of each vertex in the mesh, resulting in a smoother overall appearance. Figure 2(e) depicts this optimization process.

(6) Domain extension. Computational workload is minimized by using mesh bias to generate element sizes that gradually vary in space. Figure 2(f) demonstrates this extension technique.

(7) Fault embedding or equivalence. The fault is either incorporated as a thin separate slice within the mesh grid or the finite-thick solid elements are accounted for by calculating equivalent physical parameters.
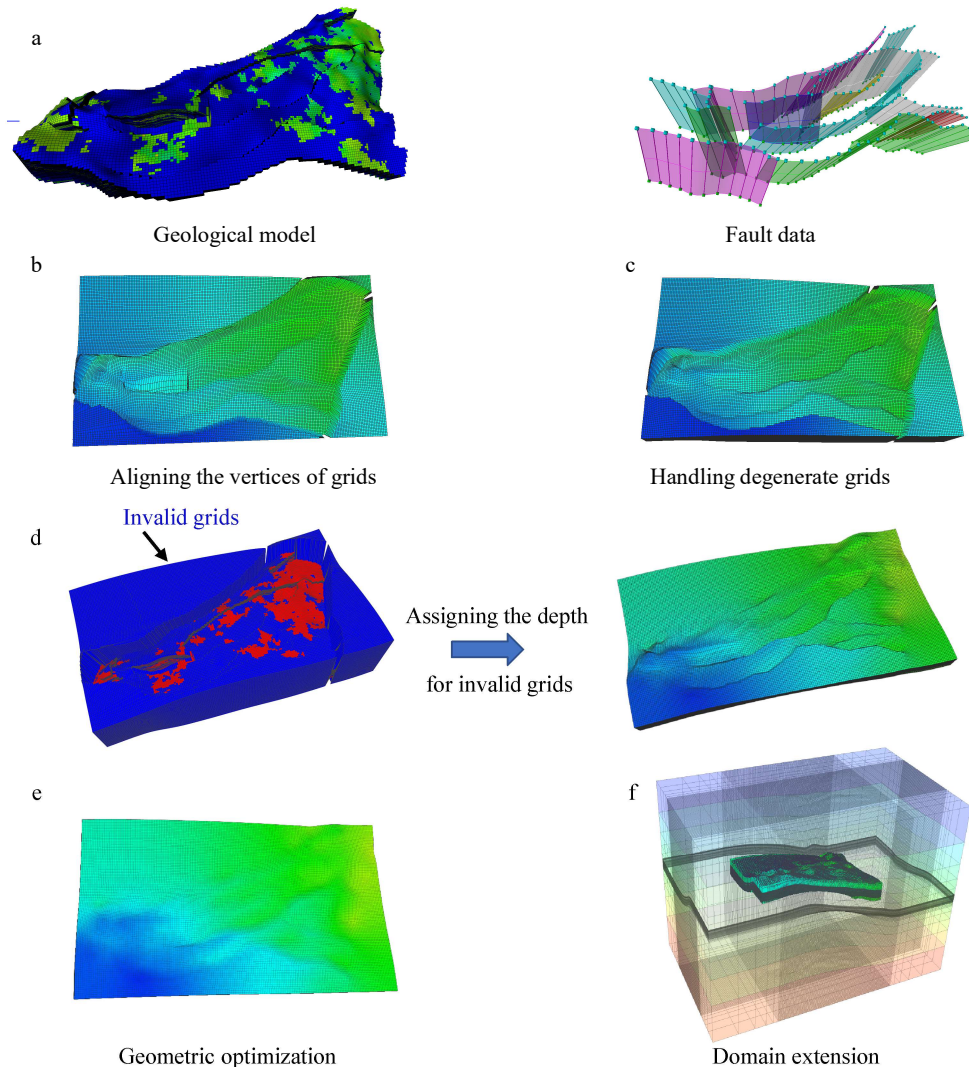

Figure 2. The work flow of establishing a full 3D filed model

Coupled Fluid and Solid Mechanics

Assuming small deformation and isothermal conditions, the deformation of a porous medium during fluid injection is mainly driven by the in-situ pore pressure, with the amount of the total displacements mainly controlled by the rock compressibility (Teatini et al. 2014). The quasi-static linear momentum equation for the solid mechanics can be written as:

$$\nabla \cdot \boldsymbol{\sigma} + \rho \mathbf{g} = 0, \tag{1}$$

where $\boldsymbol{\sigma}$ is the Cauchy total stress tensor, ρ is the bulk density for the multiphase system, and $\mathbf{g}$ is the gravitational acceleration. To account for the interaction between the fluid flow and solid deformation within the porous media, the effective stress equation is used and written as:

$$\boldsymbol{\sigma}' = \boldsymbol{\sigma} - \alpha P \boldsymbol{\delta}, \tag{2}$$

where $\boldsymbol{\sigma}'$ is the effective stress, α is the Biot's coefficient of rock saturated with water, P is the fluid pressure, and $\boldsymbol{\delta}$ is the Kronecker symbol.

To simplify the problem setting, molecular diffusion and hydrodynamic dispersion are neglected during our simulation. Assuming fluid phases remain separated within the porous media, the mass balance equation for multiphase and multicomponent flow is expressed as:

$$\phi \frac{\partial}{\partial t} \left(\sum_p S_p \rho_p X_p^\kappa \right) + \nabla \cdot \left(\sum_p \rho_p X_p^\kappa \, \boldsymbol{v}_p \right) - \sum_p \rho_p X_p^\kappa q_p = 0, \tag{3}$$

where ϕ is the porosity, S_p is the saturation of phase p, ρ_p is the density of phase p, X_p^κ is the mass fraction of component κ in phase p, $\boldsymbol{v}_p$ is the Darcy velocity of phase p, q_p is the volumetric source term of phase p, and t is the time. The Darcy velocity $\boldsymbol{v}_p$ of phase p is governed by the multiphase extension of Darcy's law,

$$\boldsymbol{v}_p = -\boldsymbol{k} \frac{k_{\mathrm{r}p}}{\mu_p} \cdot \left(\nabla P_p - \rho_p \mathbf{g} \right), \tag{4}$$

where $\boldsymbol{k}$ is the intrinsic permeability, $k_{\mathrm{r}p}$ is the relative permeability of phase p, μ_p is the viscosity of phase p.

The rock is considered compressible, so the porosity varies. According to poroelasticity theory, the porosity ϕ can be computed as:

$$\phi = \phi_0 + \alpha \left(\epsilon_v - \epsilon_{v,0} \right) + \frac{P - P_0}{N}, \tag{5}$$

where ϕ_0 is the porosity at a reference state with pressure p_0 and volumetric strain $\epsilon_{v,0}$, ϵ_v is the volumetric strain, $N = K_s / (\alpha - \phi_0)$, and K_s is the grain bulk modulus.

Mohr-Coulomb Failure Criterion

Evaluating the risk of shear failure is an important consideration when assessing the feasibility of CO_2 geological storage and ensuring the long-term integrity of the storage site. The Mohr-Coulomb criterion describes the shear failure of soil and rock, which represents a linear envelope obtained from a plot of shear strength τ against the effective normal stress σ', expressed as

$$\tau = c + \sigma' \tan \varphi, \tag{6}$$

where c is the internal cohesion and φ is the internal friction angle. The Mohr-Coulomb representation provides a schematic view of the stress state, offering a comprehensive understanding of the mechanism of shear failure. Allowable stress states corresponding to Mohr circles are those that do not intersect the Mohr-Coulomb linear failure envelope. If the stress state (Mohr's circle) touches the failure envelope, shear failure may occur, as shown in Figure 3(a). The potential for failure is provided by the safety factor χ (Teatini et al. 2014):

$$\chi = 1 - \frac{(\sigma_1' - \sigma_3')/2}{c\cos\varphi + \sin\varphi(\sigma_1' + \sigma_3')/2} = 1 - \frac{\tau_m}{\tau_m^*}, \tag{7}$$

where σ_1' and σ_3' are the maximum and minimum principal stress, respectively; τ_m and τ_m^* are the current largest and maximum allowable shear stress, respectively. Wherever χ becomes zero a shear failure is likely to occur.

The Mohr-Coulomb criterion can also be used to investigate the fault reactivation, as shown in Figure 3(b). Reactivation along pre-existing faults potentially occurs where the shear stress τ_n and the normal effective stress σ_n' acting on the fault plane (unit normal vector $\boldsymbol{n}$) do not satisfy the following bound,

$$|\tau_n| < \sigma_n' \tan \varphi_f + c_f, \tag{8}$$

where c_f and φ_f are the internal cohesion and the internal friction angle of the fault, respectively. When the shear stress on the fault plane equates or exceeds the limit, the faults can slip. Define the following Coulomb failure function ω to assess the fault stability (Teatini et al. 2014, Zoback 2007):

$$\omega = |\tau_n| - (\sigma_n' \tan \varphi_f + c_f). \tag{9}$$

If the ω is negative, indicating that the shear stress does not exceed the resistance to sliding, the fault remains stable. Conversely, as the ω approaches zero, the possibility of sliding occurring increases.
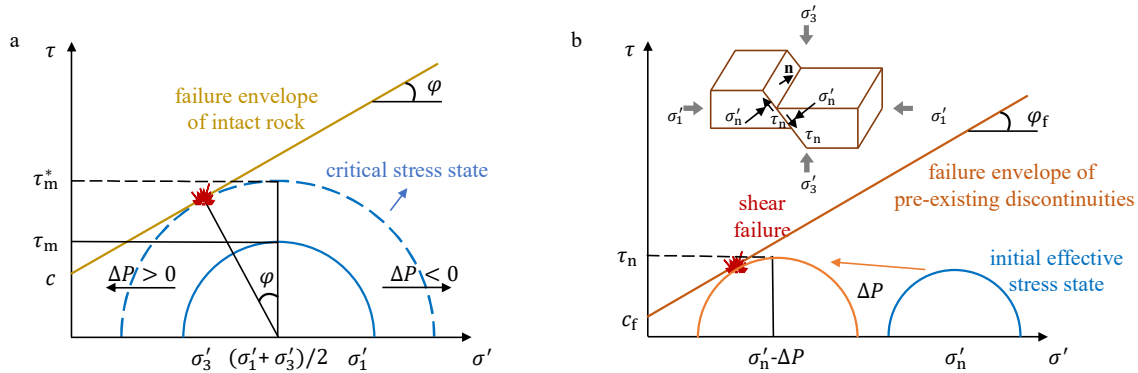

Figure 3. Shear failure criteria based on the Mohr-Coulomb strength criterion. (a) Example of Mohr's circles representing the porous medium stress state, (b) Mohr's circles showing how the reduction in effective stresses due to pressure buildup induces shear failure in faults.

Case Study of the Shengli Oilfield

Geological descriptions. The Gao89-1 block of Shengli Oilfield is the target site in this work. The Gao89-1 block is located in the northern part of the Zhenglizhuang field within the Dongying sag, which is part of the central Jinjia-Zhenglizhuang-Fanjia structural belt. This Dongying sag is situated in the western portion of the Dongying depression-Boxing sag in Shandong, eastern China. Within the Boxing sag, the Jinjia-Fanjia nose structures have developed as inherited structures, spanning the entire sag from south to north and dividing it into western and eastern segments (Wang et al. 2017). The Gao89-1 block is

bounded by faults to the north and south. It exhibits a topographically higher southwest region and a lower northeast region with a dip of 5° - 8°. The sandstone comprises approximately 40% - 60% quartz, 20% - 40% feldspar, and 10% - 20% lithic fragments (Li et al. 2017). The structure is divided into multiple terraces by a series of parallel northwest-trending and northeast-trending faults, with the largest structural gap reaching 500 m - 700 m (Bai et al. 2017). The orientation of the maximum principal stress σ_H is NE69.0°. The reservoir depth ranges from 2800 m to 3000 m with a temperature of 126 °C. The Gao89-1 block is characterized as a high-temperature, low-permeability, and heterogeneous oil reservoir with an average original porosity of 12.5% and a permeability of 4.7 mD.

Model descriptions. Based on the available geological information of the Gao89-1 block, a full 3D model is established using the method described earlier. The dimensions of the original grid are 7.28 km × 4.21 km, with a depth range of 2734 m - 3366 m, as shown in Figure 2(a). Through processing and extension, the dimensions of the grid are extended to 25 km × 16 km, encompassing a depth range of 0 m - 5000 m, as shown in Figure 4. The full 3D field model of the Gao89-1 block consists of 2,362,200 hexahedral elements, with around 770,000 cells representing the reservoir. The model consists of four distinct rock layers: caprock, reservoir, basement, and surrounding formation, while fractures and faults are equivalent to the rock matrix.

In the established full 3D field model, CO_2 is injected into the reservoir through an injection well (labeled as G89-4). The CO_2 injection is implemented as a point source, and the injection schedule remains constant rate of 50 ton/day for 10 years. However, the simulations were extended to a total duration of 30 years to capture the geohydrological and geomechanical behavior of the full field model. At the depth of injection point, initial fluid pressure and temperature (32.6 MPa and 399 K) assure supercritical conditions for CO_2. Based on the long production history of reservoirs and its current status as a depleted oil reservoir, a simplified approach is taken by adopting a two-phase (CO_2 and water) model. Furthermore, the entire system is assumed to be isothermal, neglecting any thermal effects.

Constant pressure, saturation, and temperature conditions are applied to the boundaries where no flow occurs. Null displacement conditions are set normal to the bottom and lateral boundaries, while stress is set to the top boundaries. The model is executed in a linear elastic analysis. Hydraulic and mechanical properties are given in Table 1. The rock density is 2650 Kg/m³, and the internal cohesion is neglected. The GEOS simulator (Settgast et al. 2022) is employed to simulate the CO_2 injection process and the geomechanical response. Due to the extensive number of model grid cells, the computational process involves handling a substantial amount of data. In order to enhance the efficiency of simulations, parallel computing techniques were employed.

Table 1. Parameters for numerical simulations

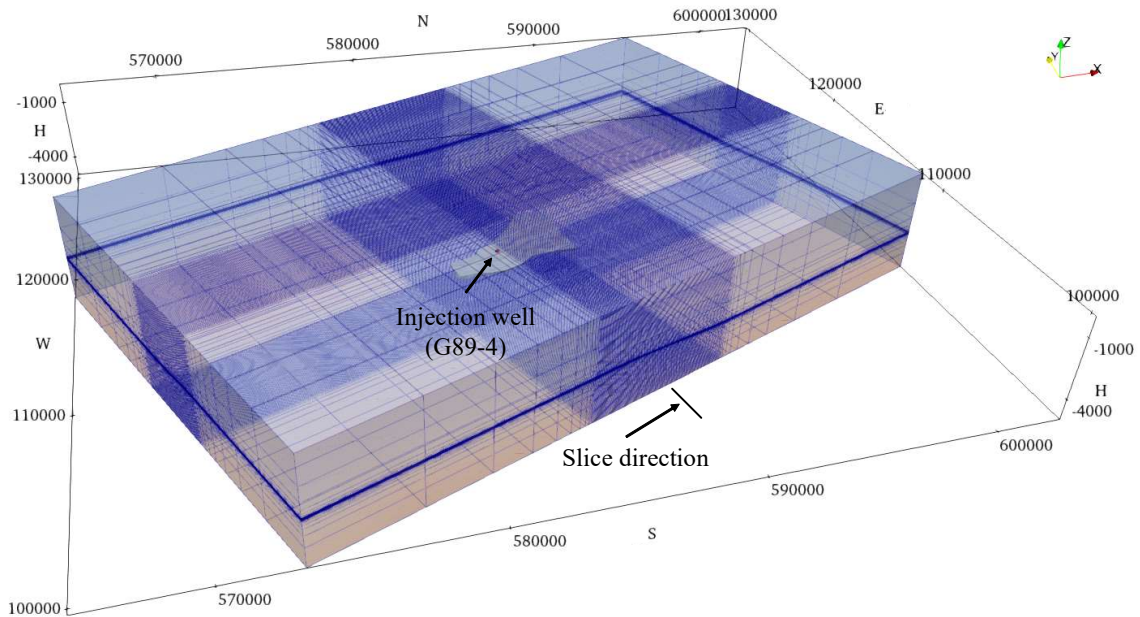|	Permeability (m²)	Porosity (%)	Poisson's ratio	Young's modulus (GPa)	Internal friction angle (°)
Caprock	1.0×10^{-16}	10	0.2	30	40
Reservoir	4.7×10^{-15}	12	0.2	20	30
Basement	1.0×10^{-16}	10	0.2	30	40
Surroundings	1.0×10^{-16}	10	0.2	30	40

Figure 4. The full 3D field model of Gao89-1 block

Numerical results and discussions. After 10 years of CO_2 injection, the simulation results for fluid pressure within the reservoir are shown in Figure 5. The changes in mean effective stress and shear stress in the cross-section of the full 3D field model are presented in Figure 6 and Figure 7, respectively. The position of the slice and perspective direction are indicated in Figure 4. A monitoring point was selected at the interface between the reservoir and caprock, located 100 m away from the injection well along the positive direction of the x-axis. In addition, three vertical lines, labeled A, B, and C, were chosen at distances of 100 m, 500 m, and 1000 m, respectively, from the injection well along the positive direction of the x-axis. Figure 8 illustrates the evolution of fluid pressure, mean effective stress, and shear stress at the monitoring point. During CO_2 injection period, the fluid pressure and shear stress gradually increase with the injection time, while the mean effective stress gradually decreases. Their peak values reach 117.66%, 110.34%, and 94.84% of the original equilibrium values, respectively. After the injection is halted, they rapidly reverse and then slowly stabilize. The stabilized values of fluid pressure, shear stress, and mean effective stress are 103.41%, 101.37%, and 98.96% of the original equilibrium values, respectively. The stabilized fluid pressure and shear stress are higher than the pre-injection equilibrium values, while the mean effective stress is lower. According to the Mohr-Coulomb criterion, the stress state at monitoring point is illustrated in Figure 9. Throughout the CO_2 injection phase, the stress state moves closer to the failure envelope, which increases the risk of shear failure. However, after the injection is stopped, the stress state undergoes a reversal but stabilizes to the left of the initial stress state

The changes in fluid pressure and mean effective stress with depth along lines A, B, and C are shown in Figure 10. The increment of shear stress with depth is shown in Figure 11. Within the reservoir, the fluid pressure increases while the mean effective stress decreases. Notably, the increase in fluid pressure surpasses the decrease in mean effective stress. During CO_2 injection, shear stress increases more significantly within the reservoir but increases more slowly in the caprock. In the post-injection period, the shear stress decreases in the reservoir and basement, but the increment is still present. Based on the calculations using Equation 7, the safety factor χ is calculated and the results at the across-section are shown in Figure 12. The values are within the range of 0.3-0.9. This indicates that the formation remains in a relatively safe and stable state, with an expected absence of shear failure. Such favorable condition

can be attributed to the implementation of a relatively low injection rate and the careful selection of simulation parameters.
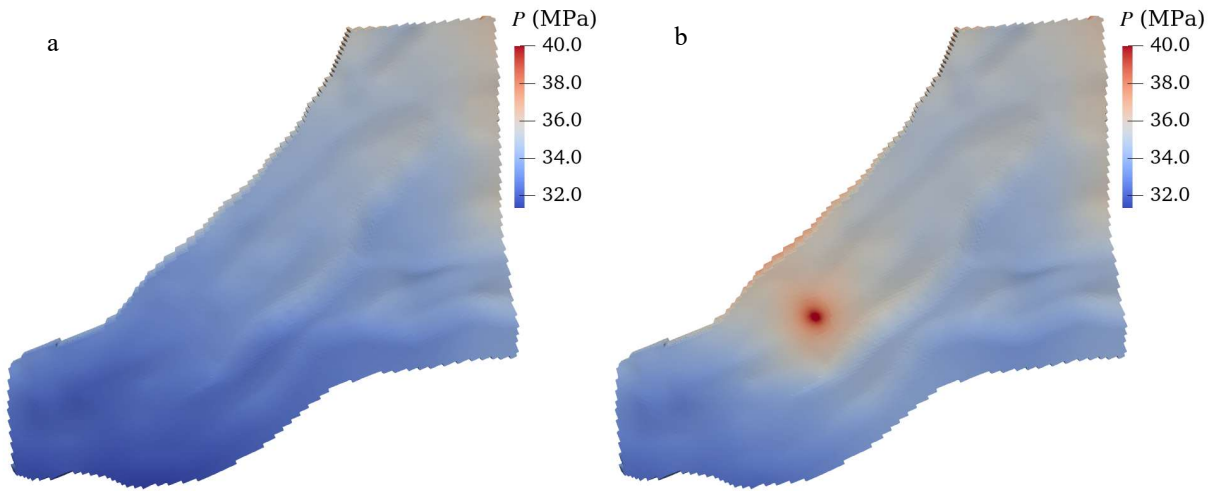

Figure 5. (a) The initial fluid pressure and (b) the fluid pressure after 10 years of injection
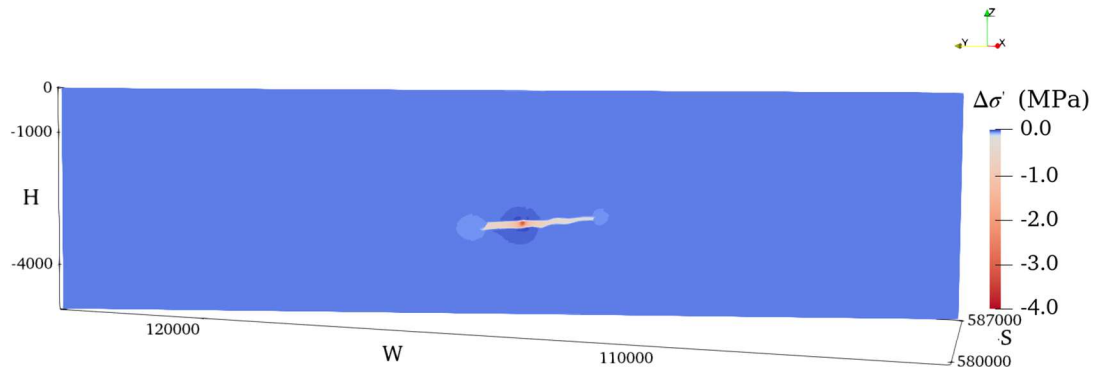

Figure 6. Change in the mean effective stress on the cross-section after 10 years of injection
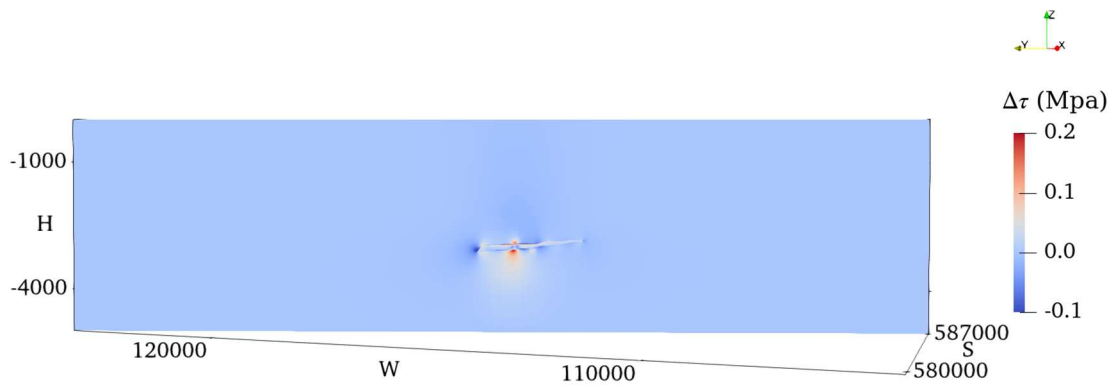

Figure 7. Change in the shear stress on the cross-section after 10 years of injection
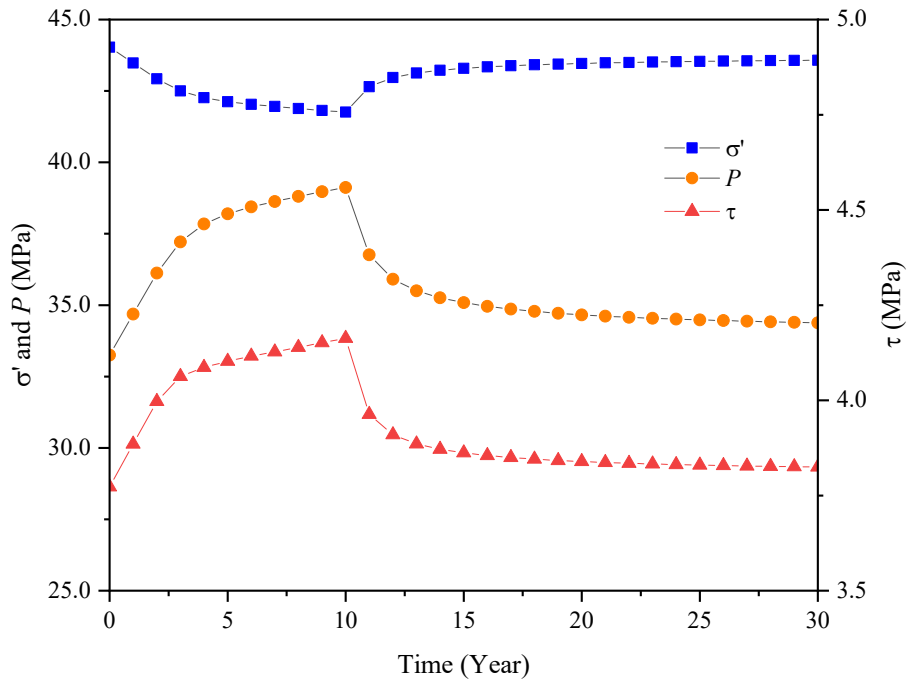
Figure 8. Evolution of fluid pressure, mean effective stress, and shear stress at monitoring point
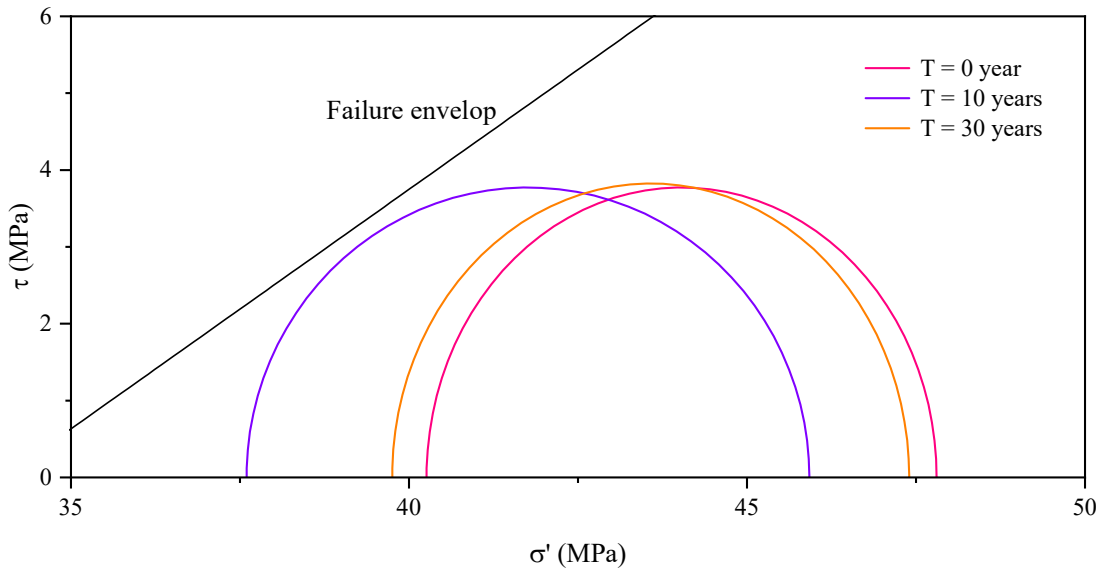

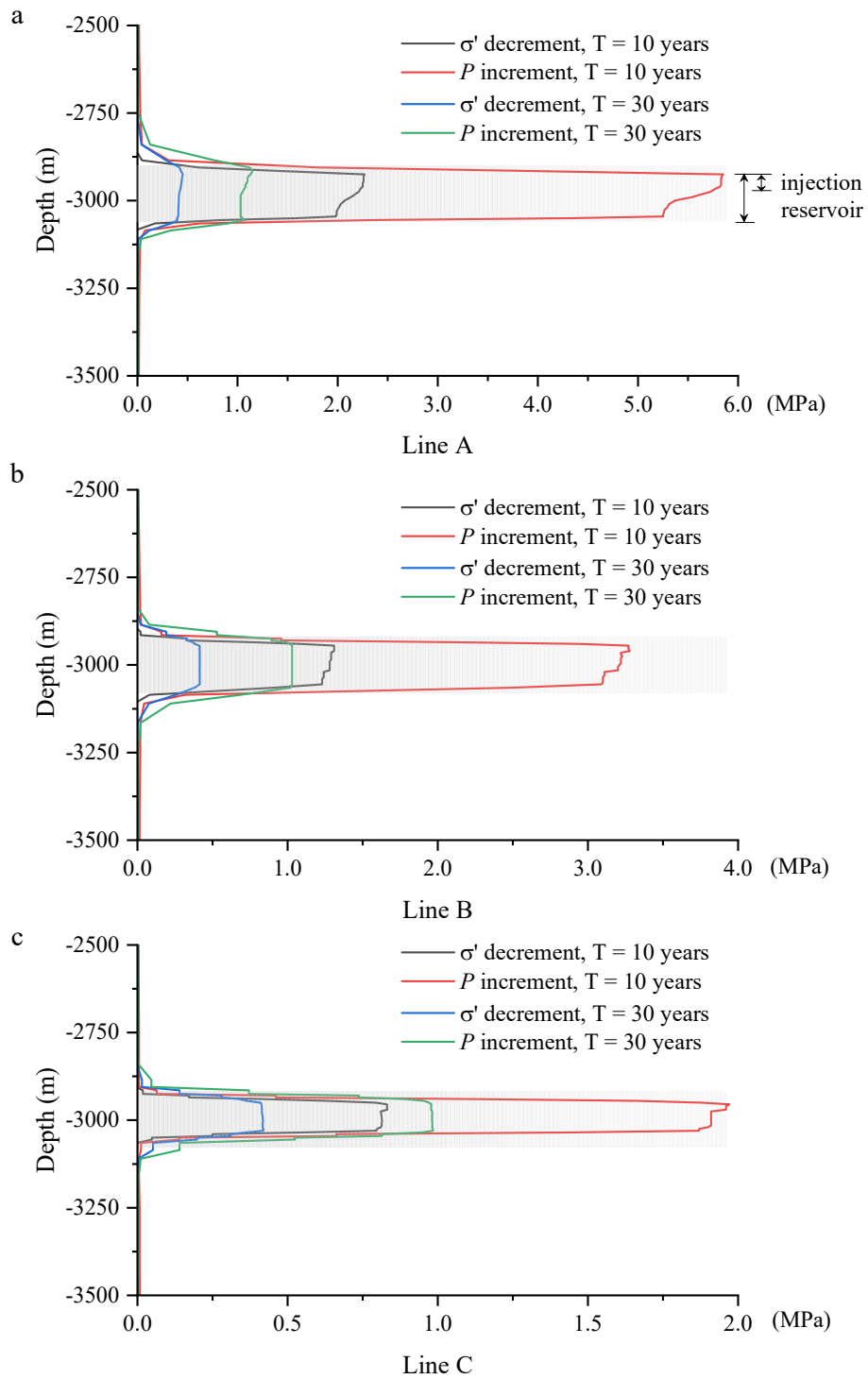Figure 9. Stress state of monitoring point at crucial time points

Figure 10. The changes in fluid pressure and mean effective stress along lines A, B, and C
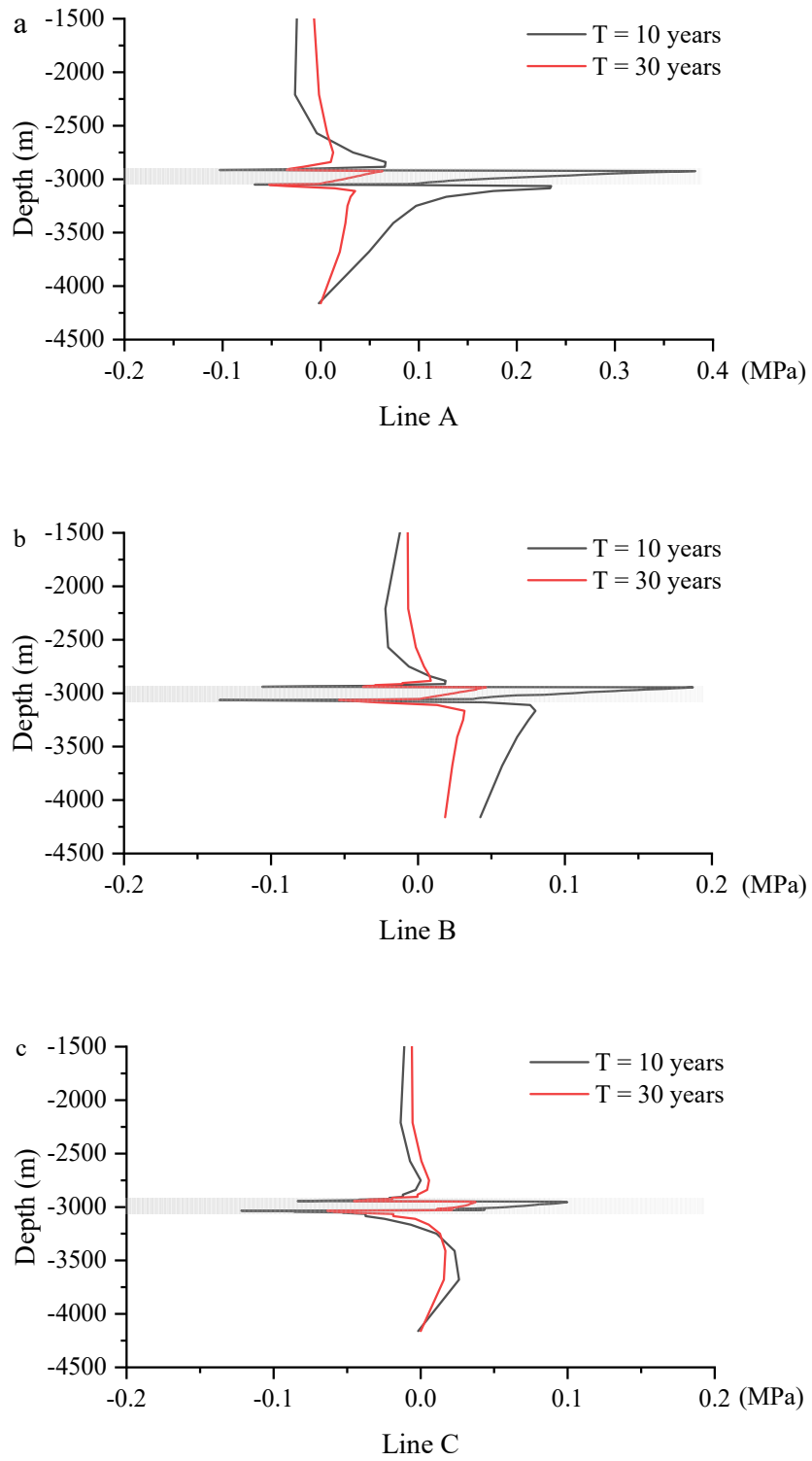
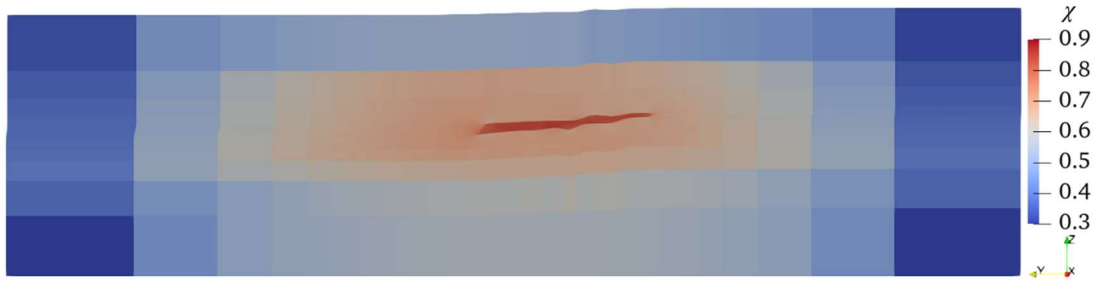Figure 11. The changes in shear stress along lines A, B, and C

Figure 12. The results of safety factor on the cross-section

Conclusions

To accurately simulate the stress distribution, it is essential to convert the corner-point grid of the target geological model into a standard finite element mesh. The establishment of a finite element grid for a full 3D field model involves reading the target reservoir model and faults data, aligning the vertices of grids, handling degenerate grids, assigning the depth for invalid grids, geometric optimization, domain extension, and fault embedding or equivalence.

During CO_2 injection, fluid pressure and shear stress gradually increase with injection time, while the average effective stress gradually decreases. After stopping injection, the stress state moves backward, but remains to the left of the initial stress state after stabilization. Caprock stability and fault reactivation are assessed based on Mohr-Coulomb failure criterion. For caprocks, safety factor is employed to assess the trend of failure. Similarly, the stability of faults is determined using the Coulomb failure function. As CO_2 is injected, the stress state tends towards the failure envelope, increasing the risk of shear failure. However, once the injection is halted, the stress state moves backward, but stabilizes to the left of the initial stress state.

Acknowledgements

References

Adu-Gyamfi, Benjamin, Ampomah, William, Tu, Jiawei et al. 2022. Assessment of chemo-mechanical impacts of CO2 sequestration on the caprock formation in Farnsworth oil field, Texas. *Scientific Reports* 12 (1). 13023. https://www.nature.com/articles/s41598-022-16990-x.pdf.

Aminu, Mohammed D., Nabavi, Seyed Ali, Rochelle, Christopher A. et al. 2017. A review of developments in carbon dioxide storage. *Applied Energy* 208: 1389-1419. https://www.sciencedirect.com/science/article/pii/S0306261917313016?via%3Dihub.

Bai, Bing, Hu, Qifang, Li, Zhipeng et al. 2017. Evaluating the Sealing Effectiveness of a Caprock-Fault System for CO2-EOR Storage: A Case Study of the Shengli Oilfield. *Geofluids*. Unsp 8536724.

Chen, Qiyu, Liu, Gang, Li, Xinchuan et al. 2017. A corner-point-grid-based voxelization method for the complex geological structure model with folds. *Journal of Visualization* 20 (4): 875-888. https://doi.org/10.1007/s12650-017-0433-7.

Hettema, Marc. 2020. Analysis of mechanics of fault reactivation in depleting reservoirs. *International Journal of Rock Mechanics and Mining Sciences* 129: 104290. https://www.sciencedirect.com/science/article/pii/S1365160919310287.

Jin, Ye-Jun, Meng, Ling-Dong, Lyu, Ding-You et al. 2023. Risk assessment of fault reactivation considering the heterogeneity of friction strength in the BZ34-2 Oilfield, Huanghekou Sag, Bohai Bay Basin, China. *Petroleum Science* 20 (5): 2695-2708. https://www.sciencedirect.com/science/article/pii/S1995822623001632.

Legentil, Capucine, Pellerin, Jeanne, Raguenel, Margaux et al. 2023. Towards a workflow to evaluate geological layering uncertainty on CO2 injection simulation. *Applied Computing and Geosciences* 18: 100118. https://www.sciencedirect.com/science/article/pii/S2590197423000071.

Li, Lin, Ma, Jin-Feng, Wang, Hao-Fan et al. 2017. Shear wave velocity prediction during CO2-EOR and sequestration in the Gao89 well block of the Shengli Oilfield. *Applied Geophysics* 14 (3): 372-380. https://doi.org/10.1007/s11770-017-0638-5.

Liu, Yu-yang, Pan, Mao, and Liu, Shi-qi. 2019. Petrel2ANSYS: Accessible software for simulation of crustal stress fields using constraints provided by multiple 3D models employing different types of grids. *Journal of Central South University* 26 (9): 2447-2463. https://doi.org/10.1007/s11771-019-4186-4.

Newell, P. and Martinez, M. J. 2020. Numerical assessment of fault impact on caprock seals during CO2 sequestration. *International Journal of Greenhouse Gas Control* 94: 102890. https://www.sciencedirect.com/science/article/pii/S1750583619302427

Pan, Pengzhi, Wu, Zhenhua, Feng, Xiating et al. 2016. Geomechanical modeling of CO2 geological storage: A review. *Journal of Rock Mechanics and Geotechnical Engineering* 8 (6): 936-947. https://www.sciencedirect.com/science/article/pii/S1674775516300580.

Raziperchikolaee, Samin and Pasumarti, Ashwin. 2020. The impact of the depth-dependence of in-situ stresses on the effectiveness of stacked caprock reservoir systems for CO2 storage. *Journal of Natural Gas Science and Engineering* 79. 103361. https://www.sciencedirect.com/science/article/pii/S1875510020302158?via%3Dihub.

Settgast, Randolph Richard, Corbett, Benjamin Curtice, Klevtsov, Sergey et al. GEOSX, https://github.com/GEOS-DEV/GEOS.

Sun, Zhuang, Salazar-Tio, Rafael, Wu, Long et al. 2023. Geomechanical assessment of a large-scale CO2 storage and insights from uncertainty analysis. *Geoenergy Science and Engineering* 224: 211596. https://www.sciencedirect.com/science/article/pii/S2949891023001835.

Teatini, Pietro, Castelletto, Nicola, and Gambolati, Giuseppe. 2014. 3D geomechanical modeling for CO2 geological storage in faulted formations. A case study in an offshore northern Adriatic reservoir, Italy. *International Journal of Greenhouse Gas Control* 22: 63-76. https://www.sciencedirect.com/science/article/pii/S1750583613004544.

Wang, Haofan, Ma, Jinfeng, Li, Lin et al. 2017. Time-lapse Seismic Analysis for Gao89 Area of CO2-EOR Project in SINOPEC Shengli Oilfield, China. *Energy Procedia* 114: 3980-3988. https://www.sciencedirect.com/science/article/pii/S1876610217317241.

Yoon, Sangcheol, Lee, Hikweon, and Kim, Jihoon. 2023. The modeling of fault activation, slip, and induced seismicity for geological CO2 storage at a pilot-scale site in the Janggi Basin, South Korea. *International Journal of Rock Mechanics and Mining Sciences* 170: 105441. https://www.sciencedirect.com/science/article/pii/S1365160923001156.

Zheng, Fangning, Jahandideh, Atefeh, Jha, Birendra et al. 2021. Geologic CO2 Storage Optimization under Geomechanical Risk Using Coupled-Physics Models. *International Journal of Greenhouse Gas Control* 110: 103385. https://www.sciencedirect.com/science/article/pii/S1750583621001377.

Zoback, Mark D. 2007. *Reservoir Geomechanics*. Cambridge: Cambridge University Press.